OPEN

Pancreatic Intraepithelial Neoplasia Revealed by Diffusion-Tensor MRI

Carlos Bilreiro, MD, Francisca F. Fernandes, MSc, Rui V. Simões, PhD, Rafael Henriques, PhD, Cristina Chavarrías, PhD, Andrada Ianus, PhD, Mireia Castillo-Martin, MD, PhD, Tânia Carvalho, DVM, PhD, Celso Matos, MD, and Noam Shemesh, PhD

Objectives: Detecting premalignant lesions for pancreatic ductal adenocarcinoma, mainly pancreatic intraepithelial neoplasia (PanIN), is critical for early diagnosis and for understanding PanIN biology. Based on PanIN's histology, we hypothesized that diffusion tensor imaging (DTI) and T2* could detect PanIN.

Materials and Methods: DTI was explored for the detection and characterization of PanIN in genetically engineered mice (KC, KPC). Following in vivo DTI, ex vivo ultrahigh-field (16.4 T) MR microscopy using DTI, T2* was performed with histological validation. Sources of MR contrasts and histological features were investigated, including histological scoring for disease burden (lesion span) and severity (adjusted score). To test if findings in mice can be translated to humans, human pancreas specimens were imaged.

Results: DTI detected PanIN and pancreatic ductal adenocarcinoma in vivo (6 KPC, 4 KC, 6 controls) with high discriminative ability: fractional anisotropy (FA) and radial diffusivity with area under the curve = 0.983 (95% confidence interval: 0.932–1.000); mean diffusivity and axial diffusivity (AD) with area under the curve = 1 (95% confidence interval: 1.000–1.000). MR microscopy with histological correlation (20 KC/KPC; 5 controls) revealed that sources of MR contrasts likely arise from microarchitectural signatures: high FA, AD in fibrotic areas surrounding lesions, high diffusivities within cysts, and high T2* within lesions' stroma. The strongest histological correlations for lesion span and adjusted score were obtained with AD ($R = 0.708$, $P < 0.001$; $R = 0.789$, $P < 0.001$, respectively). Ex vivo observations in 5 human pancreases matched our findings in mice, revealing substantial contrast between PanIN and normal pancreas.

Conclusions: DTI and T2* are useful for detecting and characterizing PanIN in genetically engineered mice and in the human pancreas, especially with AD and FA. These are encouraging findings for future clinical applications of pancreatic imaging.

Key Words: diffusion tensor imaging, carcinoma in situ, pancreatic neoplasms, pancreatic intraepithelial neoplasia, animals, genetically modified

(*Invest Radiol* 2024;00: 00–00)

Pancreatic cancer, mainly represented by ductal adenocarcinoma (PDAC), is the third leading cause of cancer-related death in the United States, with an estimated 11% survival rate at 5 years.[1] As symptoms develop late in the course of the disease, most patients are diagnosed at advanced stages precluding pancreatic resection surgery, which remains the only potentially curative therapeutic option.[2] Moreover, when patients are diagnosed in the early disease stages and subjected to tumor resection, the 5-year survival rate reaches 25%–50%.[3,4] Therefore, identifying precursor lesions for PDAC, mainly composed of pancreatic intraepithelial neoplasia (PanIN), could provide opportunities for early diagnosis and development of more effective therapies.[5,6] However, PanINs are not diagnosed by current imaging modalities, with a single study describing small cystic lesions in magnetic resonance cholangiopancreatography in a subset of patients with these lesions.[7] The absence of noninvasive diagnostic tools also prevents the investigation of PanIN's biology and tumorigenesis in humans, which remains largely unknown and mostly driven by research using genetically engineered mouse models (GEMMs) and histopathological analyses.[8–10] Therefore, there is an urgent need for developing imaging methods for PanIN diagnosis and characterization, which could enable early diagnosis before PDAC is established.

Diffusion-weighted MRI (DWI) provides insights into tissue microstructure and is routinely used for diagnosis, staging, and evaluation of response to therapy in benign and malignant diseases, mostly based on apparent diffusion coefficients (ADCs).[11–14] Given the potential of DWI, diffusion tensor imaging (DTI) was developed and explored in the clinical setting to provide a rotationally invariant representation of the diffusion process in biological tissues.[11] In the pancreas, DWI has been used in the past for characterizing benign and malignant processes, but studies exploring DTI for pancreatic disease characterization remain lacking, including for the detection of PanIN and early PDAC.[15,16]

We hypothesized that high-resolution DTI, with its ability to characterize diffusion anisotropy and sensitivity toward microarchitecture, could detect and characterize microstructural changes expected in PanIN and early PDAC. To test this hypothesis, we imaged GEMM developing PanIN and PDAC in vivo and harnessed ex vivo MR microscopy at ultrahigh field and direct histological validation to understand the sources of contrast. Similar techniques were previously successful in characterizing malignant lymph nodes with high resolution.[17,18] Here, we used 2 well-established mouse models of pancreatic cancer: KC, mostly displaying PanIN lesions, and KPC, with complete penetrance of PDAC.[19] Finally, we tested our hypothesis in human pancreas samples.

Received for publication September 12, 2024; and accepted for publication, after revision, October 11, 2024.

From the Radiology Department, Champalimaud Foundation, Lisbon, Portugal (C.B., C.M.); Champalimaud Research, Champalimaud Foundation, Lisbon, Portugal (C.B., F.F.F., R.H., C.C., A.I., M.C.-M., T.C., C.M., N.S.); Nova Medical School, Lisbon, Portugal (C.B.); i3S—Instituto de Investigação e Inovação em Saúde, Universidade do Porto, Porto, Portugal (R.V.S.); and Pathology Department, Champalimaud Foundation, Lisbon, Portugal (M.C.-M.).

Conflicts of interest and sources of funding: N.S. serves on the Scientific Advisory Board of Bruker Biospin. No other potential conflicts of interest are reported from remaining authors. Champalimaud Foundation funded this work; R.V.S.'s work was supported by H2020-MSCA-IF-2018, ref: 844776; A.I.'s work received the support of a fellowship from "La Caixa" Foundation (ID 100010434) and from the European Union's Horizon 2020 research and innovation programme under the Marie Skłodowska-Curie grant agreement no. 847648, fellowship code LCF/BQ/PI20/11760029.

Correspondence to: Noam Shemesh, PhD, Champalimaud Research, Champalimaud Foundation, Av. Brasilia 1400-038, Lisbon, Portugal. E-mail: noam.shemesh@neuro.fchampalimaud.org.

Data availability statement: The data generated in this study are available upon request from the corresponding author. Any human-derived data are completely anonymized.

Supplemental digital contents are available for this article. Direct URL citations appear in the printed text and are provided in the HTML and PDF versions of this article on the journal's Web site (www.investigativeradiology.com).

ISSN: 1536-0210/24/0000–0000
DOI: 10.1097/RLI.0000000000001142

MATERIALS AND METHODS

Ethics Statement

Animals were handled in agreement with European FELASA guidelines. Animal procedures were conducted according to European Directive 2010/63 and preapproved by institutional and national authorities. The study protocol involving human biological tissue was preapproved by the institutional ethics committee. All participants provided signed informed consent before tissue collection, and personal identity was kept private through pseudonymization in the institution's Biobank.

Genetically Engineered Mouse Models

The KC (Pdx1-Cre, LSL-Kras^{G12D}/Ptf1a-Cre, LSL-Kras^{G12D}) and KPC (Ptf1a-Cre, LSL-Kras^{G12D}, p53^{LoxP}) mouse models were used: KC mice develop PanIN and progress to PDAC; KPC mice develop PanIN and PDAC with complete penetrance.[19] Healthy mice (C57BL/6 J background) were used as controls. All animals' rearing was undertaken in a specific pathogen-free facility in a temperature-controlled room, with a 12-hour light/dark cycle with ad libitum access to food and water. The animals' cages were enriched with plastic igloos and shredded paper. Given the potential of GEMM for developing advanced pancreatic disease, the animals were continuously monitored for signs of malaise, namely, weight loss/cachexia, fur thinning, and apathetic or aggressive behavior. Whenever these signs were observed, the animals were humanely sacrificed.

Anatomical In Vivo Imaging

In a first exploratory phase (Fig. 1A), KC (n = 9) and KPC (n = 6) mice were imaged monthly from 4 months old, to assess the development onset of pancreatic abnormalities. Animals were imaged until abnormalities were observed, with a T2-weighted turbo spin-echo sequence (Table 1), in 1 T and 9.4 T scanners (respectively, Icon and BioSpec; Bruker, Germany; 40-mm ID linear transmit-receive volume coil) depending on scanner availability: 41 scans were performed in 1 T; 15 scans were performed in 9.4 T scanners. Animal characteristics are described in Table 2. Anesthesia was induced with 5% isoflurane (Vetflurane; Virbac, France) mixed with oxygen-enriched (28%) air. Isoflurane dosage was reduced to 1.5%–2.5% during animal preparation and for the duration of MRI scanning. Breathing rate and rectal temperature were monitored and recorded throughout scans using a pillow pressure sensor and an optic fiber temperature probe (SA Instruments Inc, Stony Brook, USA). A warm-water recirculating pad was used for body temperature control, maintaining rectal temperature between 35.0°C and 37.0°C. Ophthalmic gel (Vidisic Gel; Bausch+Lomb, Canada) was applied to the animals' eyes before each acquisition for preventing eye dryness. All acquisitions began with routine adjustments: center frequency, radiofrequency calibration, and automatic shimming.

In Vivo DTI Animals Selection

KPC mice presented early-onset disease with pancreatic abnormalities in anatomical T2-weighted in vivo imaging and physical signs of malaise. In contrast, KC mice presented pancreatic abnormalities later in their development. Considering these preliminary findings, we decided to use young animals from the KPC and older animals from the KC transgenic lines for this part of the study: 6 KPC, 4 KC, and 6 controls (Supplemental Digital Content 1, Table with sample characteristics, http://links.lww.com/RLI/A980), with an estimated statistical power of 0.95 ($\alpha = 0.05$; estimated effect size = 2.2). The predicted number of KC mice was 6; however, due to unexpected deaths of 2 KC mice before pancreas extraction, these animals could not be used for histopathological analysis and were excluded from the study.

In Vivo DTI

KPC (n = 6), KC (n = 4), and control (n = 6) mice were imaged in a 9.4 T scanner (BioSpec; Bruker, Germany; 40-mm ID linear transmit-receive volume coil). Intraperitoneal hyoscine butylbromide (5 mg/kg; Buscopan; Boehringer Ingelheim, Spain) was administered 8 minutes before acquisition for bowel motion reduction.[20] A diffusion-weighted spin-echo echo-planar-imaging was used for imaging the animals' abdomen (Table 1). Datasets were analyzed using in-house developed

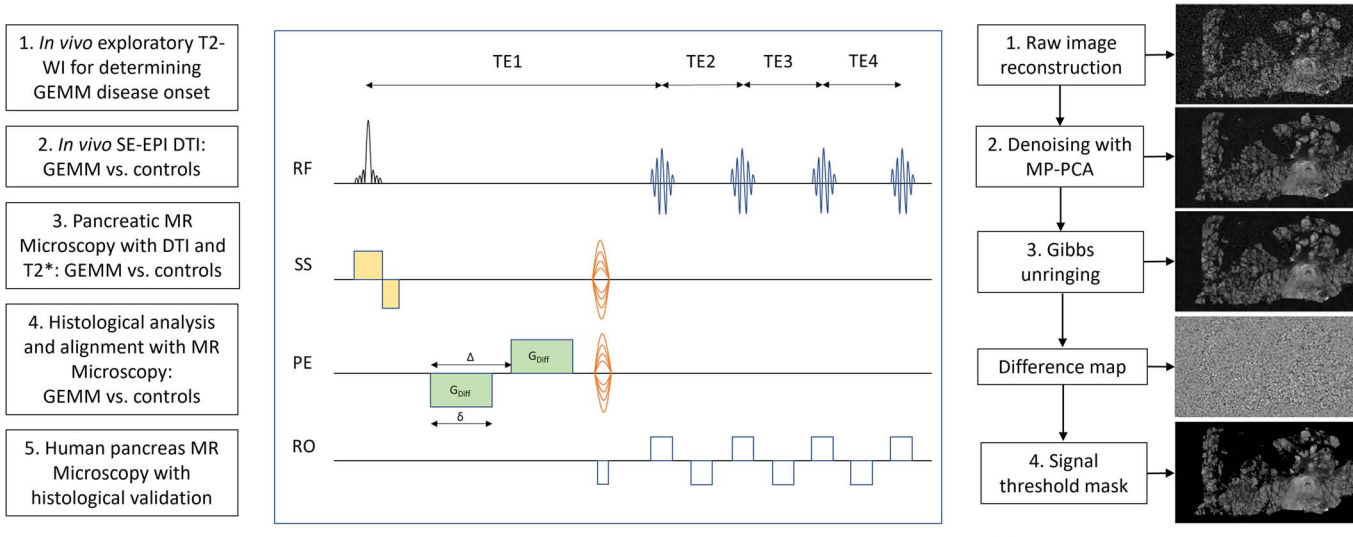

FIGURE 1. Study design, diffusion-weighted multi-gradient-echo pulse sequence diagram, and preprocessing pipeline. A, Study design with major steps performed in chronological order. B, Diffusion-weighted multi-gradient-echo sequence used for the ex vivo MRI acquisition, which includes a small flip-angle slab-selective excitation followed by diffusion gradients and phase encoding, and a multiple-gradient-echo readout echo-train (RF, radiofrequency; SS, slice selection; PE, phase encoding; RO, readout; GDiff, diffusion gradients; δ, diffusion gradient duration; Δ, diffusion time; TE2 = TE3 = TE4). C, Data preprocessing pipeline, with a respective example image obtained in each step (MP-PCA = Marchenko-Pastur principal component analysis). Difference map is the resulting subtraction of pixel values between the raw image and the processed image after denoising and unringing, displaying the removal of image noise and ringing artifacts.

TABLE 1. MRI Acquisition Parameters

Pulse Sequence	T2-TSE	SE-EPI	DMGE
Magnetic field strength	1 T; 9.4 T	9.4 T	16.4 T
In-plane resolution (mm^2)	0.150 × 0.150 (1 T) 0.125 × 0.125 (9.4 T)	0.125 × 0.125	-
Slice thickness (mm)	0.7 (1 T) 0.3 (9.4 T)	0.25	-
No. slices	20–36	36	-
3D resolution (mm)	-	-	0.08 × 0.08 × 0.08
TR (ms)	3825 (1 T) 1500–2700 (9.4 T)	2300–2600	125
TE (ms)	60 (1 T) 20–22 (9.4 T)	15.6–16.5	9.2–10.2
Signal averages	30 (1 T) 10–16 (9.4 T)	16	1
Acceleration factor	8	-	-
Multishot segments	-	4	-
Partial Fourier reduction factor	-	1.7	-
EPI sampling bandwidth (kHz)	-	395	-
Fat suppression	No	Yes	Yes
No. DTI B values	-	1	1
B values (s/mm^2)	-	1000	775–1200
No. B = 0 s/mm^2	-	2	2
Diffusion directions	-	10	10
Respiratory triggering	Yes	Yes	-
Scan duration	44–50 min (1 T) 12–21 min (9.4 T)	31–33 min	5 h 54 min–16 h 33 min

T2-TSE, T2-weighted turbo spin echo; SE-EPI, spin-echo echo planar imaging; DMGE, diffusion-weighted multi-gradient-echo.

code in MATLAB (MathWorks Inc, Natick, MA). Data preprocessing included denoising based on Marchenko-Pastur principal component analysis (MP-PCA) and Gibbs unringing.[21,22] Fractional anisotropy (FA), mean diffusivity (MD), axial diffusivity (AD), and radial diffusivity (RD) maps were produced, fitting DTI to diffusion-weighted images using a weighted-least-squares solution.[23] The images obtained were analyzed by a gastrointestinal radiologist, who segmented the entire pancreas in each slice, using MATLAB's built-in segmentation tools. Measurements obtained from pancreatic segmentation were used for groupwise comparisons. After MRI, all animals had their pancreases harvested and subjected to histopathological diagnosis, so disease status (presence of PanIN, PDAC) was known for each animal.

Pancreas Specimens' Preparation for MR Microscopy

Pancreases from additional KPC (n = 8), KC (n = 12), and control (n = 5) mice were prepared for MR microscopy. As pancreatic abnormalities were evident in T2-weighted images at 8.5 (interquartile range [IQR] = 0.75) months of age for KC mice, these animals were studied at this age (n = 12), whereas n = 8 KPC mice were studied at 4.25 (IQR = 0.25) months old, right after the first exploratory MRI scans, due to early aggressive disease.[19] Preliminary findings were used for calculating the number of animals in each group: pancreases harvested from 3 KC mice and 1 healthy control were imaged and FA maps were produced. According to a comparison of median FA measurements, effect size was estimated at 1.6, and a similar effect size was assumed for KPC mice. With a statistical power of 0.95, each animal group was initially aimed at 10 animals. However, due to unpredictable events when developing the colonies, 12 KC (available surplus in litter production) and 8 KPC mice were finally used (3 KPC mice suffered premature deaths and their pancreases could not be harvested on time). GEMM and n = 5 controls were sacrificed with cervical dislocation, and their pancreases dissected and removed through median laparotomy. Pancreatic specimens were subjected to fixation: immersion in

TABLE 2. Sample Characteristics in Anatomical Longitudinal T2-Weighted Imaging of GEMM

Animal Model	KC	KPC
No. animals	9	6
Pancreatic abnormalities onset (months old)	8.5 (IQR = 0.75)	4.25 (IQR = 0.25)
Animal weight (g)	30.4 (IQR = 11.2)	22.9 (IQR = 4.1)
Animal sex	4/9 females	4/6 females

Continuous variables expressed as medians and IQR. Pancreatic abnormalities onset was assessed from 4 months old.

TABLE 3. Lesion Adjusted Score Calculation, Adapted From Veite-Schmahl et al[25] and Basturk et al[26]

Score	Grade	Distribution
1	Low-grade	Focal
2	High-grade	Multifocal
3	PDAC	Diffuse

The final adjusted score for each pancreatic specimen was determined using the following distribution-adjusted lesion grade = (low-grade × distribution) + (high-grade × distribution) + (PDAC × distribution).

4% paraformaldehyde for 48 hours and then in phosphate-buffered saline with 0.01% sodium azide for 24 hours. After fixation, pancreases were immersed in Fluorinert within a 10-mm NMR tube for ex vivo MRI, with special care for removing air bubbles and animal hair in the sample.

Ex Vivo MR Microscopy

Pancreases were imaged in a 16.4 T MRI scanner (Ascend Aeon; Bruker, Germany), using a diffusion-weighted multi-gradient-echo sequence, providing ultrahigh-resolution 3D images with both diffusion and T2* weighting (Fig. 1B, Table 1).[24] Two 10-mm probes were used (Micro5, Cryoprobe; Bruker, Germany) depending on availability; sample temperature was maintained at 37°C. Datasets were preprocessed as previously described (MP-PCA denoising, Gibbs unringing, Fig. 1C).[21,22] After preprocessing, images were masked to remove low-signal areas. T2*, DTI (FA, MD, AD, RD), and ADC maps were then obtained from the preprocessed datasets.[23]

Histological Analysis

Following MRI, mouse pancreas samples were serially sectioned (4-µm thickness, 0.5-mm spacing) and stained with hematoxylin and eosin. Slides were digitally scanned in Ultra-Fast Scanner (Philips) or AxioScan Z1 (Zeiss) and examined by a veterinary pathologist.

The classification of pancreatic lesions—acinar-to-ductal metaplasia (ADM), low-grade PanIN, high-grade PanIN, and PDAC—was based on specific criteria (Supplemental Digital Content 2, Table with classification, http://links.lww.com/RLI/A980), adapted from Veite-Schmahl et al[25] and Basturk et al.[26] Disease severity scoring was performed on the slide where the extent of the lesions was higher. A distribution-adjusted lesion grade with equal contribution from each lesion type was developed, ensuring that all lesions contribute equally to the final score, rendering a continuous range of scores, adapted from Berman-Booty et al[27] and Knoblaugh and Himmel.[28] This system calculates the score by summing the product of the scores for grade and distribution of each lesion, as shown in Table 3: distribution-adjusted lesion grade = (low-grade PanIN × distribution) + (high-grade PanIN-distribution) + (PDAC × distribution) with ascribed scores of 1, 2, and 3 for low-grade PanIN, high-grade PanIN, and PDAC, respectively, and for focal, multifocal, and diffuse lesions, respectively. The same histological slide was also used to calculate lesion span (ie, lesion burden for each specimen), through digital segmentation using QuPath v. 0.4.3 semimanual segmentation tools, by annotating area of the lesions and area of normal pancreas.[28,29]

Lesion span and adjusted score were correlated with MRI data, assessing if DTI and T2* measurements scale with disease extension and severity.

Imaging and Histology Alignment

The alignment between MRI and histology was manually performed by a gastrointestinal radiologist. For this, the Volume Viewer tool from ImageJ (US National Institutes of Health) was used for reconstructing the 3D datasets in real time and searching for image planes corresponding to histology slides using the powder-averaged diffusion-weighted images. Specimens' structures (lymph nodes, large blood vessels, cystic lesions, and large masses) were used as landmarks for searching for the most adequate image plane. When the manually reconstructed image plane and slice were deemed the most approximate as possible to the corresponding histological slide, the reconstruction coordinates were used in all DTI and T2* maps, and the corresponding images were exported for a visual comparison between both histology and MRI. Image contrasts were therefore attributed to the corresponding histological changes, as directly observed.

Human Pancreas

Pancreas specimens (n = 5) obtained from patients with PDAC, from the institution's Biobank (formalin-fixed leftovers after diagnostic procedures following resection surgery), were analyzed searching for PanIN.[30] Specimens were sliced and placed inside a 10-mm MR tube. Sample preparation, imaging acquisition, and processing methods described above for MR microscopy were used. Histological slides were sectionized, stained,

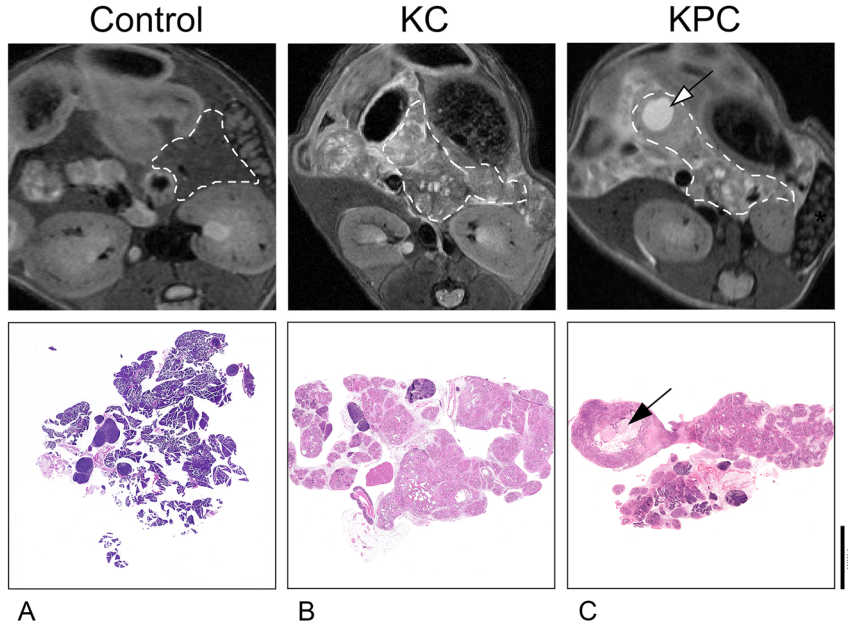

FIGURE 2. Pancreatic abnormalities with cystic changes are seen in vivo in KPC (4.75 months old) and KC (8.5 months old) mice, using conventional TSE-T2-weighted images, with corresponding histological diagnosis, including acinar-to-ductal metaplasia, PanIN, and PDAC lesions. The healthy control (2 months old) pancreas is homogeneous without focal or diffuse changes. C, A necrotic/cystic area inside a large tumor (arrows) is directly correlated with histology. All 3 images were acquired in a 9.4 T scanner (BioSpec).

and digitized, as described above, and evaluated by a gastrointestinal pathologist. Alignment was performed manually by a gastrointestinal radiologist, as previously described, for a visual comparison.

Statistical Analysis

IBM SPSS statistics v.23 was used. Kolmogorov-Smirnov test was used to assess the distribution of continuous variables, revealing nonnormal distributions throughout. Kruskal-Wallis test was used for groupwise comparisons, with post hoc pairwise comparisons, and Mann-Whitney *U* test for comparisons between 2 groups. Bonferroni correction was applied when comparing multiple test metrics, namely, different DTI, T2*, and ADC maps, by multiplying the *P* values by the number of metrics. Receiver operating characteristics analysis was performed for assessing the discriminative value of DTI. Pearson correlation coefficient was used for evaluating MRI measurements and lesion span/adjusted score. All tests were bilateral; *P* values <0.05 were considered significant.

RESULTS

Longitudinal MRI Assessment of PanIN and PDAC Development Onset

Exploratory anatomical in vivo T2-weighted images revealed variably enlarged pancreases with high signal intensity and cystic lesions for GEMM, whereas the pancreas of control mice was homogeneous with low signal intensity (Fig. 2A). These findings were evident at 8.5 months old for KC mice and at first scans (4.25 months old) for KPC mice (Table 2), as confirmed with histopathology (Fig. 2B).

DTI Noninvasively Detects PanIN and PDAC In Vivo

Both KC and KPC mice presented pancreases with high FA, MD, AD, and RD; large PDAC; and small cystic lesions, contrasting visually with control mice which presented low values in the pancreas in all parameters (Fig. 3A).

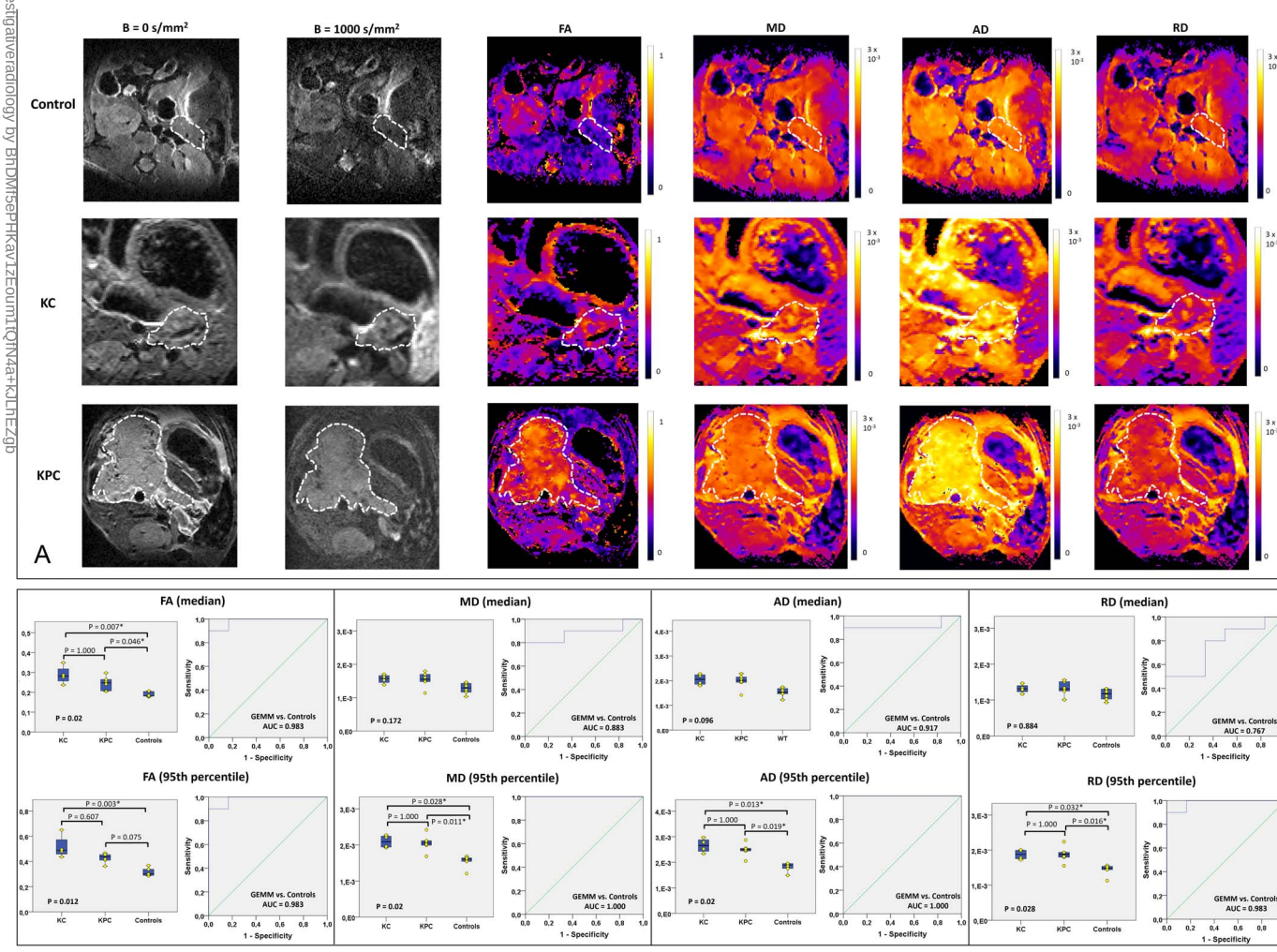

FIGURE 3. DWIs (averaged b = 0 and b = 1000 s/mm^2 images) and DTI maps (FA, MD, AD, RD) for representative KC, KPC, and healthy control mice. A, The maps produced with DTI showcase the differences between healthy controls, KC, and KPC mice. The KC presented here, with diffuse PanIN infiltration in the pancreatic parenchyma and no PDAC, has visually increased values in DTI derived maps, especially FA and AD. The KPC mouse is bearing a large PDAC, also with increased values in the same maps. In contrast, the healthy control mouse has a homogeneous pancreas with intermediate-low values in all maps. B, Quantitatively, the differences between groups of animals, including 10 GEMM (6 KPC and 4 KC) and 6 controls, provide a good discriminative ability of DTI-derived metrics. FA presents the best performance when using median values (AUC = 0.983); AD and MD present the best performance when using 95th percentile values (AUC = 1). MD, AD, RD expressed in mm^2/s.

TABLE 4. In Vivo DTI With KC and KPC Mice—Presence of PDAC

PDAC	Present	Absent	*P*
No. animals	7	3	-
Models	KC: 1/4 KPC: 6/6	KC: 3/4 KPC: 0	0.033*
FA (median)	0.25	0.28	0.833
FA (95th percentile)	0.45	0.48	0.383
MD (median)	1.6E-3	1.5E-3	1.000
MD (95th percentile)	2.1E-3	2.0E-3	0.517
AD (median)	2.1E-3	1.9E-3	0.517
AD (95th percentile)	2.5E-3	2.5E-3	0.833
RD (median)	1.3E-3	1.3E-3	1.000
RD (95th percentile)	1.9E-3	1.8E-3	0.517

Continuous variables were expressed as medians.

Fisher exact test was used for comparing prevalence of PDAC in GEMM models.

Mann-Whitney *U* test was used for comparing GEMM with and without PDAC for each DTI metric.

*Statistically significant results.

Median FA obtained after pancreatic segmentation was significantly higher for both transgenic mice (n = 6 KPC, n = 4 KC) compared with controls (n = 6), with differences increasing and becoming significant also for MD, AD, and RD, when assessing the higher values observed in each group (ie, 95th percentile) (Fig. 3B). The discriminative performance of median DTI measurements obtained from the entire pancreas in each animal for differentiating GEMM from controls was high, ranging from 0.767 (95% confidence interval [CI]: 0.527–1.000) area under the curve (AUC) for RD, up to 0.983 (95% CI: 0.932–1.000) AUC for FA. The discriminative performance increased once more when assessing the parameters' 95th percentile, with AUC ranging from 0.983 (FA and RD, 95% CI: 0.932–1.000) to 1.000 (MD and AD, 95% CI: 1.000–1.000) (Fig. 3B). When comparing KC and KPC mice, the DTI metrics were similar between both groups of animals. Also, DTI metrics could not distinguish between GEMM with (n = 7) and without PDAC (n = 3) (Table 4).

MR Microscopy With DTI and T2* Characterizes Ex Vivo Pancreatic Abnormalities

To better understand the contrasts observed, we performed detailed MR microscopy and histology in pancreases harvested from KC mice (n = 12), KPC mice (n = 8), and healthy control mice (n = 5) (Supplemental Digital Content 3, Table with sample characteristics, http://links.lww.com/RLI/A980).

After alignment between MR microscopy and histology slides, enabling a direct comparison of MRI and histology, stark contrasts between DTI and T2* parameters in normal and abnormal tissue were observed (Fig. 4). High FA values are observed in areas of ADM, where PanIN lesions of variable degrees are found surrounded by fibrosis, as well as at the periphery of PDAC lesions. In contrast, areas of normal parenchyma demonstrate low FA values, allowing a clear distinction between different types of tissue. The MD, AD, RD, and ADC maps reveal high values in cystic and necrotic areas, most evident in AD maps, and intermediate/high AD values in fibrotic areas of ADM, PanIN, and PDAC. T2* maps present high values in the stroma of both PanIN and PDAC lesions. All the control pancreases show homogeneous FA, diffusivities, T2*, and ADC maps with lower values throughout the pancreatic parenchyma.

Quantitatively, as observed for in vivo DTI, DTI/T2* maps obtained from pancreas specimens allowed us to distinguish between GEMM and controls (Fig. 5; Supplemental Digital Content 4, Figure with all group comparisons, http://links.lww.com/RLI/A981). When comparing KPC and controls, median values were significantly different, with KPC presenting higher values for MD (+10.6%, $P = 0.004$), AD (+22%, $P = 0.001$), and RD (+7.7%, $P = 0.023$). When comparing KC and controls, only median AD was different (+14%, $P = 0.046$). The comparison of highest values in each specimen (95th percentile) enhanced the observed differences between GEMM and controls. For KPC versus controls, except for FA ($P = 0.128$), KPC presented higher MD (+41.2%, $P = 0.006$), AD (+45.4%, $P = 0.0018$), RD (+38.9%, $P = 0.004$), T2* (+69.6%, $P = 0.017$), and ADC (+43.2%, $P = 0.005$). For KC versus controls, KC presented higher FA (+186.7%, $P = 0.003$), MD (+38.2%, $P = 0.006$), AD (+47.5%, $P = 0.002$), RD (+35.7%, $P = 0.015$), T2* (+58.6%, $P = 0.010$), and ADC (+40.8%, $P = 0.006$). When comparing KC and KPC, no differences were observed for median or 95th percentile values; however, the lowest values (5th percentile) were lower in KC for MD (−15.8%, $P = 0.003$), AD (−14.4%, $P = 0.007$), and RD (−15.2%, $P = 0.005$). Variable median ADC for different diffusion directions in each animal further demonstrates diffusion anisotropy in the pancreas (Supplemental Digital Content 5, Figure with median ADC for all diffusion directions, http://links.lww.com/RLI/A982).

Histologically, ADM was present in all GEMM mice, most markedly in KC mice, as shown in Supplemental Digital Content 6 (Figure, representative segmented samples, http://links.lww.com/RLI/A983) and Table 5 (all samples). PDAC was mainly observed in KPC mice: 33.33% of KC and 87.5% of KPC mice. Both GEMM had PanIN lesions of grades 1 to 3, more marked in KC mice. Most mice had ≥70% of their pancreas affected: 75% of KC mice and 75% of KPC mice. The median lesion span in KC mice was 80.88% (IQR: 42.75) and in KPC mice was 91.45% (IQR: 36.62). Median adjusted score was 17 (IQR: 9) in KC mice and 26 (IQR: 1.75) in KPC mice.

DTI and T2* Correlate With Disease Burden and Severity

As seen in Figure 5, Supplemental Digital Content 7 (http://links.lww.com/RLI/A984), 8 (http://links.lww.com/RLI/A985) (Figures, lesion span and adjusted score correlation plots), and 9 (Table, lesion span and adjusted score correlation coefficients, http://links.lww.com/RLI/A980), DTI/T2* metrics correlate both with disease burden (lesion span) and severity (adjusted score), when using median and 95th percentile values. The highest correlation coefficients both for lesion span and for adjusted score were obtained with AD (median AD, $R = 0.789$; 95th percentile AD, $R = 0.729$; respectively). Other than FA and T2*, 5th percentile values of MRI metrics were not correlated with histological scores.

PanIN in the Human Pancreas Revealed by Ex Vivo DTI

Human pancreas samples (Supplemental Digital Content 10, Table with patient characteristics, http://links.lww.com/RLI/A980) presented relevant histological differences when compared with the GEMM counterparts: scattered foci of ADM, higher proportion of normal pancreatic parenchyma, and absence of PDAC (Fig. 6, Supplemental Digital Content 11, http://links.lww.com/RLI/A986). In 3 samples, parenchymal atrophy with fatty replacement was observed (Figs. 6B and C, Supplemental Digital Content 11B, http://links.lww.com/RLI/A986). After alignment between MR microscopy and histology, we observed clear contrasts between areas of ADM, PanIN, and surrounding normal pancreas. High FA, AD, and T2* values were observed in areas of ADM and surrounding PanIN lesions; contrast between lesions and surrounding parenchyma was evident in all maps. One pancreas sample with diffuse interstitial fibrosis, attributed to chronic pancreatitis, showed mid-high FA, AD, and T2* values irregularly scattered throughout the fibrotic tissue (Fig. 6C). Histologically, this diffuse interstitial fibrosis is haphazardly organized, whereas the periductal fibrosis forms a

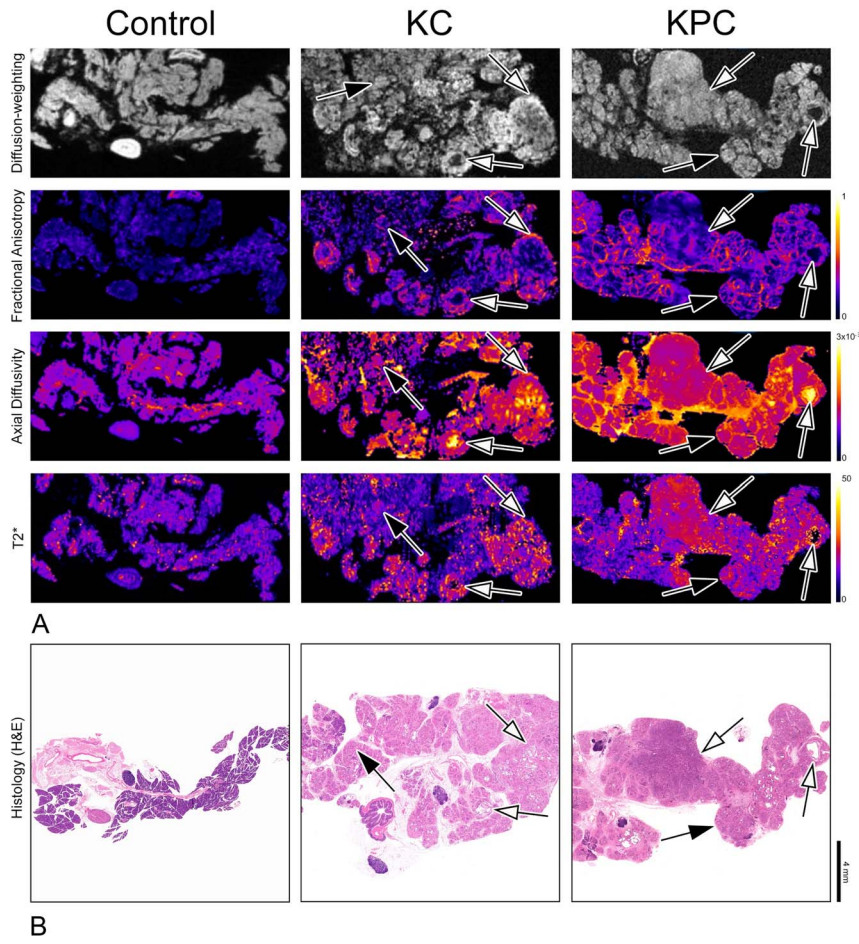

FIGURE 4. Comparison between MR microscopy and histology in GEMM. A, The healthy mouse pancreas is homogeneous, with low anisotropy, diffusivity, and T2* values; coil used: Cryoprobe. B, KC pancreas with extensive ADM and PanIN (black arrows), as well as PDAC (white arrows). Conventional diffusion weighting shows heterogeneous restricted diffusion. There are high anisotropy values in the periphery of areas with ADM, PanIN, and PDAC. High axial diffusivity is observed in cystic/necrotic areas, and intermediate diffusivity and high T2* values are seen in the lesions' stroma. Coil used: Cryoprobe. C, KPC pancreas with extensive PDAC (white arrows) and small areas of ADM and PanIN (black arrows). Conventional diffusion weighting is not helpful in delineating the pancreatic lesions. There are high anisotropy values in the periphery of PDAC and PanIN lesions; high diffusivity values in cystic/necrotic areas and regions with inflammatory infiltrates; and high T2* values in the lesions' stroma. Coil used: Micro5. AD is expressed in mm^2/s; T2* is expressed in milliseconds (ms).

sheath or cuff-like structure around ducts in areas of ADM, PanIN, and PDAC.

DISCUSSION

This study provides evidence establishing a potential role for DTI and T2* in characterizing PanIN and PDAC. We report that ex vivo and in vivo MRI detects PanIN-associated changes and PDAC, identifying potential mechanisms for the contrast and underscoring their translational relevance for imaging the human pancreas.

The process of carcinogenesis in PDAC follows a progressive development of PanIN, where genetic mutations and morphological changes are acquired until PDAC is finally established.[10,31] There is a recognized absence of noninvasive detection methods for PanIN, precluding research into PanIN biology, especially in humans.[7,32] Most current knowledge of PanIN was achieved with studies performed in GEMM.[9,31] Thus, the development of noninvasive detection methods can not only inform about PanIN biology and tumorigenesis, but also provide opportunities for early therapeutic interventions or close follow-up of patients, enabling PDAC diagnosis in resectable stages. Here, we leverage GEMM for DTI detection of PanIN, PDAC, and associated pancreatic changes, suggesting DTI/T2* as potential biomarkers for disease onset, staging, or monitoring. Our results also highlight the important variability between pancreatic structural changes in these models, probably caused by variable proportions of tumoral stroma, ductal structures, and inflammatory infiltrates, which should be accounted for in future studies.

The DTI and T2* maps provided more striking visual contrasts than conventional diffusion-weighted images, the method currently used in clinical practice. As observed by comparing MRI with histology, these contrasts appear to be derived from specific microstructural characteristics of the lesions: areas of anisotropy with high FA values corresponded to the peripheral zones of PanIN, ADM, and PDAC, where sheath/cuff-like periductal fibrosis is observed; areas of high diffusivities corresponded mostly to cystic and necrotic regions; areas of high T2* corresponded mostly to stromal components. Also, AD performed better than other metrics, including the clinical standard ADC, for lesion detection and correlated more closely with disease extent and severity. These results hint to differences in tissue microstructure

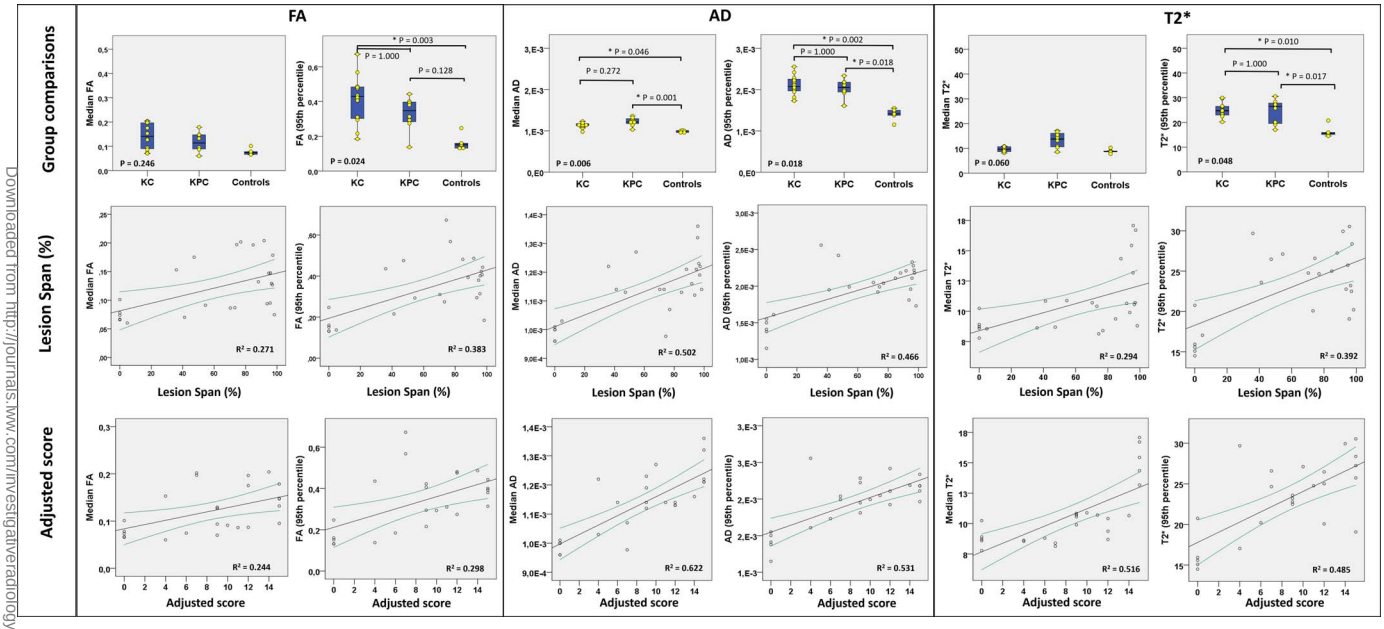

FIGURE 5. Group comparisons, lesion span, and adjusted score for DTI (FA and AD are shown) and T2* metrics. For group comparisons, the differences between GEMM and controls are highlighted when using the highest (95th percentile) values, where AD provided the largest differences. For lesion span correlation, the use of 95th percentile values improved the results, where AD was the most correlated metric. For adjusted score, both medians and the 95th percentile values showed significant correlations with disease burden and severity, but the 95th percentile values did not show an improvement when compared with median values. Again, AD provided the best performance (R^2 = 0.622, when using the median values). The group comparisons, lesion span, and adjusted score correlations for all MRI metrics can be found in Supplemental Digital Content 4, 7, and 8.

as the origin of the observed MRI contrasts and highlight the value of microstructural characterization through DTI, as previously described for other applications.[13,33,34]

PanIN remains an elusive lesion in humans. Noncommunicating pancreatic microcysts in magnetic resonance cholangiopancreatography were reported to predict the presence of PanIN in pancreatic specimens, with 61% accuracy.[7] Our findings show that DTI/T2* might be useful in this context, as the contrasts seen in human pancreas allowed a clear detection of PanIN. Regarding differentiation between degrees of PanIN and PDAC, we found a clear correlation between disease burden and severity and DTI/T2* metrics; however, the visual contrasts were mostly similar, both in vivo and ex vivo. This may question the specificity of DTI/T2* for visually differentiating low-grade from high-grade PanIN and PDAC, but further data are needed to address this question.

The presence of parenchymal atrophy with fatty replacement has been reported previously, as a finding associated with PanIN and early PDAC.[7,35,36] Our findings in human pancreas specimens corroborate these reports, with 3 out of 5 samples presenting fatty replacement. This was not observed on GEMM, however, as the animals' pancreases presented with increased size and parenchymal replacement by abnormal tissue. The presence of fatty tissue is not observed in our DTI/T2* data, as the acquisitions were performed with fat suppression, and no fat-sensitive pulse sequences were performed. The characterization of fatty replacement is an interesting point for future studies, especially if performed on the human pancreas.

DTI has been performed successfully for imaging the pancreas in clinical context.[16] However, its clinical role remains undetermined, both for PDAC detection/characterization and for characterizing other malignant lesions or nonmalignant pancreatic processes. Technical differences between MRI in basic research and clinical imaging are obvious, and pulse sequence adaptations with loss of resolution are expected due to hardware constraints in clinical scanners and time constraints when imaging patients. For PanIN detection, information loss with lower resolutions in 1.5 T and 3 T scanners might be overcome with the use of pulse sequences sensitive to microscopic anisotropy.[37] Future studies should investigate if DTI can be used in clinical context for PanIN detection and characterization, addressing the question of specificity for high- and low-grade PanIN and PDAC, as this issue is most

TABLE 5. Histological Analysis of KC, KPC, and Control Mice Used for MR Microscopy

Animal Model	Controls	KC	KPC
ADM	0%	100% (12/12)	100% (8/8)
Low-grade PanIN	0%	100% (12/12)	100% (8/8)
High-grade PanIN	0%	100% (12/12)	100% (8/8)
PDAC	0%	33.33% (4/12)	87.5% (11/12)
Lesion span (%)	0%	80.88 (IQR = 42.75)	91.45 (IQR = 36.62)
Adjusted score	0	17 (IQR = 9)	26 (IQR = 1.75)

Low-grade PanIN includes PanIN 1 and PanIN 2. Continuous variables expressed as medians and IQR.

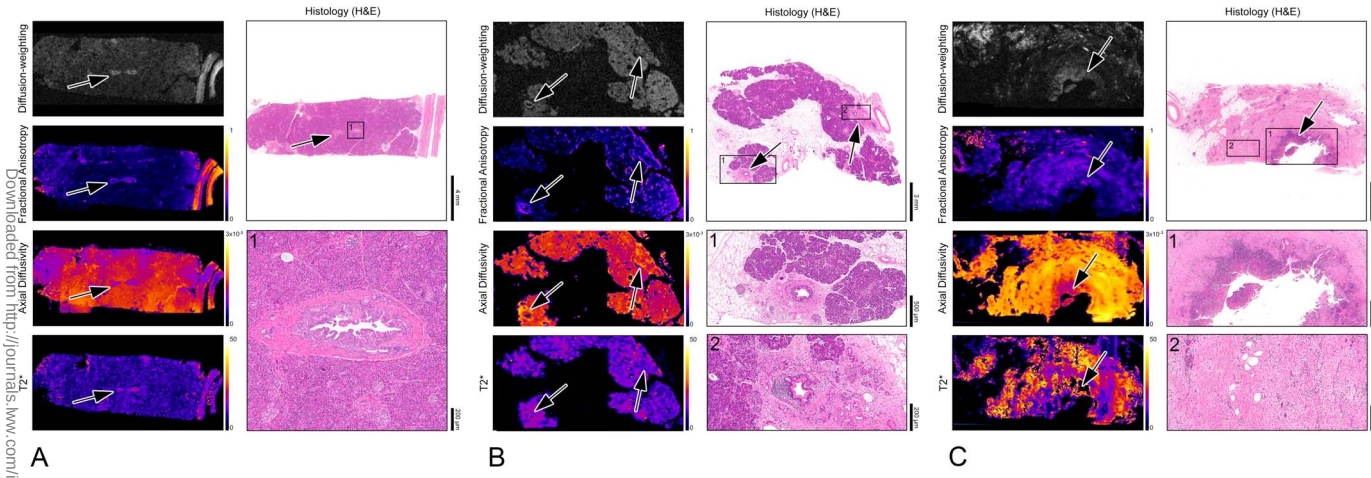

FIGURE 6. The contrasts observed with MR microscopy DTI in the human pancreas are similar to the ones seen in GEMM (2 remaining specimens are presented in Supplemental Digital Content 11). A, High anisotropy, high T2*, and low AD are seen in the periphery of a high-grade PanIN lesion, contrasting well with the surrounding normal pancreatic parenchyma (arrows). B, As observed previously in the KC/KPC mice, areas with ADM and low-grade PanIN have high anisotropy and AD values at their periphery, with high T2* values in the stroma (arrows). Large areas of fatty tissue are seen in the specimen. C, This specimen has extensive haphazardously deposited fibrotic deposition and fatty infiltration, consistent with chronic pancreatitis. There are low-grade PanIN with high anisotropy, intermediate AD, and T2* values (arrows), but the fibrosis has heterogeneous anisotropy, higher AD, and T2* values. Some areas of this specimen have irregular T2* values, probably due to fixation artifacts. AD is expressed in mm^2/s; T2* is expressed in milliseconds (ms).

relevant for implementing therapeutic interventions. Eventual combinations of DTI with other diagnostic tools could be used for increasing specificity, such as liquid biopsy and artificial intelligence.[38,39] Also, it would be interesting to investigate if DTI could be used in conjunction with 3D histological mapping, for detecting specific genomic profiles of PanIN and PDAC.[8] Multiparametric MRI could also be studied for characterizing premalignant lesions, harnessing information from different pulse sequences and including diffusion-based techniques like intravoxel incoherent motion, which have already demonstrated feasibility.[40–42]

We acknowledge some limitations of this research work. First, GEMM do not fully recapitulate morphological and biological features of human PanIN and PDAC, as PanIN lesions in the mouse are mostly present in the context of extensive ADM. Nevertheless, the observed image contrasts are useful for in vivo animal imaging, and large similarities with human pancreas samples were observed, suggesting relevance for human imaging. Second, the manual alignment between MRI and histology was suboptimal and could be considered a potential source of errors, as automatic registration was not viable due to the expected distortion and configurational changes during sample processing for histology. Third, the in vivo application developed here demonstrates the feasibility of the technique and its usefulness for differentiating GEMM from healthy controls but did not evaluate its role in determining different degrees of disease progression in vivo. Also, KC and KPC mice were observed in different age groups due to their different rates of disease progression. Future studies evaluating animals of the same transgenic line at different stages of disease progression should elucidate if DTI is useful for determining the stage of disease in similar age groups. Finally, although similarities of imaging contrasts were observed when imaging human pancreas samples, it remains to be determined if DTI can be successfully adapted to clinical scanners for imaging patients and maintain sensitivity toward these lesions. Our work provides exciting data in this regard and is encouraging for the development of clinical DTI applications for pancreatic imaging.

In conclusion, PanIN lesions were detected with DTI and T2* contrast in GEMM and human pancreas, suggesting high relevance as noninvasive biomarkers. This augurs well for characterizing PanIN progression and biology and associated pancreatic changes in both mice and humans.

ORCID ID

Noam Shemesh *https://orcid.org/0000-0001-6681-5876*

REFERENCES

1. Siegel RL, Miller KD, Fuchs HE, et al. Cancer statistics, 2022. *CA Cancer J Clin*. 2022;72:7–33.
2. Ducreux M, Cuhna AS, Caramella C, et al. Cancer of the pancreas: ESMO clinical practice guidelines for diagnosis, treatment and follow-up. *Ann Oncol*. 2015;26 (Suppl 5):v56–v68.
3. Campbell F, Smith RA, Whelan P, et al. Classification of R1 resections for pancreatic cancer: the prognostic relevance of tumour involvement within 1 mm of a resection margin. *Histopathology*. 2009;55:277–283.
4. Springfeld C, Ferrone CR, Katz MHG, et al. Neoadjuvant therapy for pancreatic cancer. *Nat Rev Clin Oncol*. 2023;20:318–337.
5. Ryan DP, Hong TS, Bardeesy N. Pancreatic adenocarcinoma. *N Engl J Med*. 2014;371:1039–1049.
6. Overbeek KA, Goggins MG, Dbouk M, et al. Timeline of development of pancreatic cancer and implications for successful early detection in high-risk individuals. *Gastroenterology*. 2022;162:772–785.e4.
7. Vullierme M-P, Menassa L, Couvelard A, et al. Non-branched microcysts of the pancreas on MR imaging of patients with pancreatic tumors who had pancreatectomy may predict the presence of pancreatic intraepithelial neoplasia (PanIN): a preliminary study. *Eur Radiol*. 2019;29:5731–5741.
8. Braxton AM, Kiemen AL, Grahn MP, et al. 3D genomic mapping reveals multifocality of human pancreatic precancers. *Nature*. 2024. Published online May 1, 2024:;629:679–687.
9. Alonso-Curbelo D, Ho YJ, Burdziak C, et al. A gene-environment-induced epigenetic program initiates tumorigenesis. *Nature*. 2021;590:642–648.
10. Storz P, Crawford HC. Carcinogenesis of pancreatic ductal adenocarcinoma. *Gastroenterology*. 2020;158:2072–2081.
11. Nilsson M, Englund E, Szczepankiewicz F, et al. Imaging brain tumour microstructure. *Neuroimage*. 2018;182:232–250.
12. Koh DM, Collins DJ. Diffusion-weighted MRI in the body: applications and challenges in oncology. *AJR Am J Roentgenol*. 2007;188:1622–1635.
13. Kiselev VG, Körzdörfer G, Gall P. Toward quantification: microstructure and magnetic resonance fingerprinting. *Invest Radiol*. 2021;56:1–9.
14. Fukukura Y, Kanki A. Quantitative magnetic resonance imaging for the pancreas. *Invest Radiol*. 2024;59:69–77.
15. Lanzman RS, Wittsack HJ. Diffusion tensor imaging in abdominal organs. *NMR Biomed*. 2017;30.
16. Nissan N, Golan T, Furman-Haran E, et al. Diffusion tensor magnetic resonance imaging of the pancreas. *PloS One*. 2014;9:e115783.

17. Santiago I, Santinha J, Ianus A, et al. Susceptibility perturbation MRI maps tumor infiltration into mesorectal lymph nodes. *Cancer Res*. 2019;79:2435–2444.
18. Ianuş A, Santiago I, Galzerano A, et al. Higher-order diffusion MRI characterization of mesorectal lymph nodes in rectal cancer. *Magn Reson Med*. 2020;84: 348–364.
19. Ariston Gabriel AN, Jiao Q, Yvette U, et al. Differences between KC and KPC pancreatic ductal adenocarcinoma mice models, in terms of their modeling biology and their clinical relevance. *Pancreatology*. 2020;20:79–88.
20. Bilreiro C, Fernandes FF, Andrade L, et al. Effective bowel motion reduction in mouse abdominal MRI using hyoscine butylbromide. *Magn Reson Med*. 2021; 86:2146–2155.
21. Kellner E, Dhital B, Kiselev VG, et al. Gibbs-ringing artifact removal based on local subvoxel-shifts. *Magn Reson Med*. 2016;76:1574–1581.
22. Veraart J, Novikov DS, Christiaens D, et al. Denoising of diffusion MRI using random matrix theory. *Neuroimage*. 2016;142:394–406.
23. Veraart J, Sijbers J, Sunaert S, et al. Weighted linear least squares estimation of diffusion MRI parameters: strengths, limitations, and pitfalls. *Neuroimage*. 2013;81: 335–346.
24. Harkins K, Does M. GitHub - remmi-toolbox/remmi-matlab: Matlab toolbox to reconstruct and process MRI data. Available at: https://github.com/remmi-toolbox/remmi-matlab. Accessed December 2, 2022.
25. Veite-Schmahl MJ, Rivers AC, Regan DP, et al. The Mouse Model of Pancreatic Cancer Atlas (MMPCA) for classification of pancreatic cancer lesions: a large histological investigation of the Ptf1aCre/+;LSL-KrasG12D/+ transgenic mouse model of pancreatic cancer. *PloS One*. 2017;12:e0187552.
26. Basturk O, Hong SM, Wood LD, et al. A revised classification system and recommendations from the Baltimore consensus meeting for neoplastic precursor lesions in the pancreas. *Am J Surg Pathol*. 2015;39:1730–1741.
27. Berman-Booty LD, Sargeant AM, Rosol TJ, et al. A review of the existing grading schemes and a proposal for a modified grading scheme for prostatic lesions in TRAMP mice. *Toxicol Pathol*. 2012;40:5–17.
28. Knoblaugh SE, Himmel LE. Keeping score: semiquantitative and quantitative scoring approaches to genetically engineered and xenograft mouse models of cancer. *Vet Pathol*. 2019;56:24–32.
29. Bankhead P, Loughrey MB, Fernández JA, et al. QuPath: open source software for digital pathology image analysis. *Sci Rep*. 2017;7:16878.
30. Andea A, Sarkar F, Adsay VN. Clinicopathological correlates of pancreatic intraepithelial neoplasia: a comparative analysis of 82 cases with and 152 cases without pancreatic ductal adenocarcinoma. *Mod Pathol*. 2003;16:996–1006.
31. Storz P. Acinar cell plasticity and development of pancreatic ductal adenocarcinoma. *Nat Rev Gastroenterol Hepatol*. 2017;14:296–304.
32. Wood LD, Canto MI, Jaffee EM, et al. Pancreatic cancer: pathogenesis, screening, diagnosis, and treatment. *Gastroenterology*. 2022;163:386–402.e1.
33. Alexander DC, Dyrby TB, Nilsson M, et al. Imaging brain microstructure with diffusion MRI: practicality and applications. *NMR Biomed*. 2019;32:e3841.
34. Gholizadeh N, Greer PB, Simpson J, et al. Characterization of prostate cancer using diffusion tensor imaging: a new perspective. *Eur J Radiol*. 2019;110: 112–120.
35. Toshima F, Watanabe R, Inoue D, et al. Ct abnormalities of the pancreas associated with the subsequent diagnosis of clinical stage I pancreatic ductal adenocarcinoma more than 1 year later: a case-control study. *Am J Roentgenol*. 2021;217: 1353–1364.
36. Sotozono H, Kanki A, Yasokawa K, et al. Value of 3-T MR imaging in intraductal papillary mucinous neoplasm with a concomitant invasive carcinoma. *Eur Radiol*. 2022;32:8276–8284.
37. Szczepankiewicz F, Lasič S, van Westen D, et al. Quantification of microscopic diffusion anisotropy disentangles effects of orientation dispersion from microstructure: applications in healthy volunteers and in brain tumors. *Neuroimage*. 2015;104:241–252.
38. Kenner B, Chari ST, Kelsen D, et al. Artificial intelligence and early detection of pancreatic cancer: 2020 summative review. *Pancreas*. 2021;50:251–279.
39. Heredia-Soto V, Rodríguez-Salas N, Feliu J. Liquid biopsy in pancreatic cancer: are we ready to apply it in the clinical practice? *Cancers (Basel)*. 2021;13.
40. Gurney-Champion OJ, Froeling M, Klaassen R, et al. Minimizing the acquisition time for intravoxel incoherent motion magnetic resonance imaging acquisitions in the liver and pancreas. *Invest Radiol*. 2016;51:211–220.
41. Concia M, Sprinkart AM, Penner A-H, et al. Diffusion-weighted magnetic resonance imaging of the pancreas: diagnostic benefit from an intravoxel incoherent motion model-based 3 b-value analysis. *Invest Radiol*. 2014;49:93–100.
42. Baskaya F, Lemainque T, Klinkhammer B, et al. Pathophysiologic mapping of chronic liver diseases with longitudinal multiparametric MRI in animal models. *Invest Radiol*. 2024;59:699–710.